



# Growth and Raman Scattering Investigation of a New 2D MOX Material: YbOCl

Yuyu Yao, Yu Zhang, Wenqi Xiong, Zhenxing Wang,\* Marshet Getaye Sendeku, Ningning Li, Junjun Wang, Wenhao Huang, Feng Wang, Xueying Zhan, Shengjun Yuan, Chao Jiang, Congxin Xia,\* and Jun He\*

MOX (M = Fe, Co, Mn, Cr, Lanthanide, or Actinide metals; O = oxygen, X = F, Cl, Br, I), an emerging type of 2D layered materials, have been theoretically predicted to possess unique electronic and magnetic properties. However, 2D MOX have rarely been investigated. Herein, for the first time, ultrathin high-quality ytterbium oxychloride (YbOCl) single crystals are successfully synthesized via an atmospheric pressure chemical vapor deposition method. Both theoretical simulations and experimental measurements are utilized to systematically investigate the Raman properties of 2D YbOCl nanosheets. The experimentally observed  $E_g$  mode at  $85.53\text{ cm}^{-1}$  and  $A_{1g}$  mode at  $138.17\text{ cm}^{-1}$  demonstrate a good match to the results from density functional theory calculations. Furthermore, the temperature-dependent and thickness-dependent Raman scattering spectra reveal the adjacent layers in YbOCl nanosheets show a relatively weak van der Waals interaction. Additionally, the polarized-dependent Raman scattering spectra show the intensity of  $A_{1g}$  mode exhibits twofold patterns while the intensity of the  $E_g$  mode remains constant as the rotation angle changes. These findings could provide the first-hand experimental information about the 2D YbOCl crystals.

metal dichalcogenides (TMDs),<sup>[10–12]</sup> and other few star materials.<sup>[13,14]</sup> However, these star materials still face great challenges in relatively low electronic performance, instability, and inefficient production, which limit their practical applications in the future. Recently, the 2D layered oxygenated compounds with fantastic properties have also stirred up research interests. For example, 2D  $\text{Bi}_2\text{O}_2\text{Se}$  crystal owns excellent performance, including high Hall mobility, high-performance flexibility, and high air stability, signifying its great potential in the applications of ultrafast, flexible optoelectronic devices.<sup>[15–17]</sup>

Being a striking family member of 2D layered materials, MOX (M = Fe, Co, Mn, Cr, Lanthanide, or Actinide metals; O = oxygen, X = F, Cl, Br, I) have been theoretically predicted to own intriguing electronic and magnetic properties.<sup>[5]</sup> For instance, monolayer chromium oxyhalide

(CrOX; X = Cl or Br) have been identified as intrinsic ferromagnetic semiconductors with Curie temperatures of up to 160 and 129 K, respectively, making 2D CrOX an excellent platform for fundamental magnetic investigation and future spintronic applications.<sup>[18]</sup> BiOCl nanosheets/ $\text{TiO}_2$  nanotube arrays heterojunction with ultrahigh on/off ratio and remarkable detectivity, can be used as high-performance UV photodetector.<sup>[19]</sup> However, so far the synthesis, properties, and applications of MOX have been rarely experimentally studied.

## 1. Introduction

In recent years, 2D layered materials, with strong chemical bonds in intralayer and relatively weak van der Waals (vdWs) force in interlayer, have attracted worldwide attention due to their potential applications for next-generation electronic and optoelectronic devices.<sup>[1–4]</sup> Although more than 5600 materials are classified as layered materials,<sup>[5]</sup> current researches of 2D layered materials primarily focus on graphene,<sup>[6–9]</sup> transition

Y. Yao, Dr. Y. Zhang, Prof. Z. Wang, M. G. Sendeku, N. Li, J. Wang, W. Huang, Dr. F. Wang, X. Zhan, Prof. C. Jiang, Prof. J. He  
CAS Center for Excellence in Nanoscience  
CAS Key Laboratory of Nanosystem and Hierarchical Fabrication  
National Center for Nanoscience and Technology  
Beijing 100190, China  
E-mail: wangzx@nanoctr.cn; hej@nanoctr.cn

Y. Yao, Prof. Z. Wang, N. Li, J. Wang, W. Huang, Prof. J. He  
Center of Materials Science and Optoelectronics Engineering  
University of Chinese Academy of Sciences  
Beijing 100049, China

The ORCID identification number(s) for the author(s) of this article can be found under <https://doi.org/10.1002/adfm.201903017>.

DOI: 10.1002/adfm.201903017

Y. Yao, N. Li  
Sino-Danish College  
University of Chinese Academy of Science  
Beijing 100049, China

W. Xiong, Prof. S. Yuan  
Key Laboratory of Artificial Micro- and Nano-Structures  
of Ministry of Education  
School of Physics and Technology  
Wuhan University  
Wuhan 430072, China

Prof. C. Xia  
Department of Physics  
Henan Normal University  
Xinxiang 453007, China  
E-mail: xiacongxin@htu.edu.cn

Recently, layered ytterbium oxychloride (YbOCl), as a member of MOX family, has been predicted to be a metal with ferromagnetic performance.<sup>[5]</sup> However, to the best of our knowledge, the preparation and basic properties of YbOCl crystal are not yet explored. Herein, for the first time, we report the controllable synthesis of 2D ultrathin single-crystalline YbOCl nanosheets via atmospheric pressure chemical vapor deposition (APCVD) method. Both hexagonal and triangular-shaped YbOCl crystals having an ultrathin thickness that approaches to sub-10 nm are obtained on sapphire substrates. High-resolution transmission electron microscopy (HRTEM) characterization and selected-area electron diffraction (SAED) pattern exhibit perfect lattice arrangement with only one set of diffraction spots, highly indicating its high crystal quality and single-crystalline structure. Furthermore, a systematic Raman study is performed on YbOCl single crystal from both theoretical and experimental perspectives. The observed  $E_g$  at  $85.53\text{ cm}^{-1}$  and  $A_{1g}$  modes at  $138.17\text{ cm}^{-1}$  are in remarkably agreement with the calculated results by density functional theory (DFT). Moreover, the temperature-dependent and thickness-dependent Raman scattering spectra reveal adjacent layers in YbOCl nanosheets are held together by the relatively weaker vdWs interactions. The polarized-dependent Raman scattering spectra show the intensity of  $A_{1g}$  mode exhibits twofold patterns as the rotation angle changes while the intensity of  $E_g$  mode keeps constant. We believe our findings would provide the fresh insights in experimental information of the 2D YbOCl material.

## 2. Results and Discussions

### 2.1. Growth and Characterizations of 2D YbOCl

YbOCl single crystal, belonging to the  $D_{3d}$  point group, possesses a trigonal space group ( $R\bar{3}m$ ) with lattice parameters of  $a = b = 3.726\text{ \AA}$ , and  $c = 27.830\text{ \AA}$ . **Figure 1a** schematically shows the crystal structure of monolayer YbOCl. It can be seen that YbOCl crystallizes in a vdWs layered structure, which is constructed by repeating sextuple layers of Cl-Yb-O-O-Yb-Cl.<sup>[20]</sup> The monolayer of YbOCl single crystal corresponds to one Cl-Yb-O-O-Yb-Cl layer with the thickness of  $9.28\text{ \AA}$  (Figure S1, Supporting Information). The top-view of YbOCl crystal structure is presented in Figure 1b, which can be viewed as a single  $[Yb_4O]$  tetrahedral unit. Yb atom forms the skeleton of the structure, and O atom occupies its interstice. Additionally, the electronic band structure of monolayer and bulk YbOCl crystal are computed using DFT calculation (Figure S2, Supporting Information), which are in accordance with the previously reported results.<sup>[5]</sup> During the APCVD growth process,  $Yb_2O_3$  and  $YbCl_3 \cdot 6H_2O$  powders were used as the precursors for the synthesis of YbOCl single crystals on sapphire ( $Al_2O_3$  (0001)) substrate which has an atomically flat surface and good thermostability. Notably, pure  $Yb_2O_3$  powder needs an excessively high temperature for the evaporation due to the extremely high melting point of  $2346\text{ }^\circ\text{C}$ , which is difficult for the conventional CVD system. Interestingly, molten salts have recently been proved to increase the vapor pressure of metal precursors and then reduce the energy barrier, so it will decrease the melting

point of metal precursors, leading to the successful synthesizing YbOCl crystals, which have been employed in the synthesis of various TMDs.<sup>[21]</sup> Similarly, in this typical experiment, the  $Yb_2O_3$  powder, evenly mixed with  $YbCl_3 \cdot 6H_2O$  powder and a small amount of sodium chloride (NaCl), was placed at the center of quartz tube. The sapphire substrate was lay face down on the mixed precursors and the YbOCl nanosheets were deposited at the temperature of  $730\text{--}800\text{ }^\circ\text{C}$ . More experimental details can be found in the Experimental Section. Figure 1c demonstrates the typical optical microscopy (OM) image of as-grown YbOCl nanosheet on the sapphire substrate, showing a regular triangle with the edge length of  $\approx 23\text{ }\mu\text{m}$ . The corresponding atomic force microscope (AFM) image (inset of Figure 1c) reveals that the thickness can be as low as  $\approx 6.6\text{ nm}$ , which is the first time to obtain such a thin YbOCl crystal. Additionally, both truncated triangular and hexagonal-shaped YbOCl nanosheets are also obtained (Figure S3, Supporting Information). Further, X-ray diffraction (XRD) was employed to identify the crystal structure of as-grown samples. As shown in Figure 1d, five main XRD peaks corresponding to the (003), (006), (009), (0012), and (0018) planes are well matched to the standard YbOCl pattern (PDF#49-1802), indicating the formation of single-crystalline YbOCl. Furthermore, HRTEM and SAED analysis were conducted on the YbOCl nanosheets to investigate the detailed atomic structure and crystallinity. The as-synthesized YbOCl nanosheets were first transferred onto carbon-supported copper grids through a polymethyl methacrylate (PMMA) assisted transfer method and then characterized by TEM. As shown in Figure 1e, the HRTEM image of a triangular YbOCl nanosheet displays a perfect atomic arrangement. The calculated lattice plane spacing of two planes with  $30^\circ$  interfacial angle are  $\approx 0.186$  and  $0.326\text{ nm}$ , which corresponds to the (110) and  $(0\bar{3}0)$  planes, respectively. More importantly, the corresponding SAED pattern (inset of Figure 1e) shows only one set of hexagonal diffraction spots, further validates its perfect high crystal quality and single-crystalline structure. And the energy dispersive spectrometer (EDS) maps (Figure S4, Supporting Information) present the uniform spatial distribution of the Yb, O, and Cl atoms in YbOCl triangle reflected by the color contrasts, which again indicate the formation of YbOCl crystals and the compositional uniformity. The rough quantification of each elements in atomic percentage as shown in Table S1 (Supporting Information). In addition, the chemical state and chemical composition of as-synthesized YbOCl nanosheets can be determined by X-ray photoelectron spectroscopy (XPS) (Figure 1f–h). The two peaks at  $189.9$  and  $186.2\text{ eV}$  clearly indicate the existence of Yb  $4d_{5/2}$  and Yb  $4d_{7/2}$  of YbOCl crystals, respectively, whereas the peak located at  $531.5\text{ eV}$  is assigned to O 1s. The chemical states of Cl  $2p_{1/2}$  and Cl  $2p_{3/2}$  can be identified from the peaks at binding energies of  $\approx 201.3$  and  $\approx 199.7\text{ eV}$ , respectively.

Additionally, the structure of as-grown hexagonal YbOCl nanosheets was also studied in detail by TEM, as shown in **Figure 2**. The TEM results emphasize that both hexagonal and triangular-shaped YbOCl nanosheets have identical crystal structure with the high-crystalline quality. And the EDS maps of Figure 2d–f further show the uniform chemical composition of hexagonal YbOCl nanosheets, and the atomic percentages of each elements are listed in Table S2 (Supporting Information).

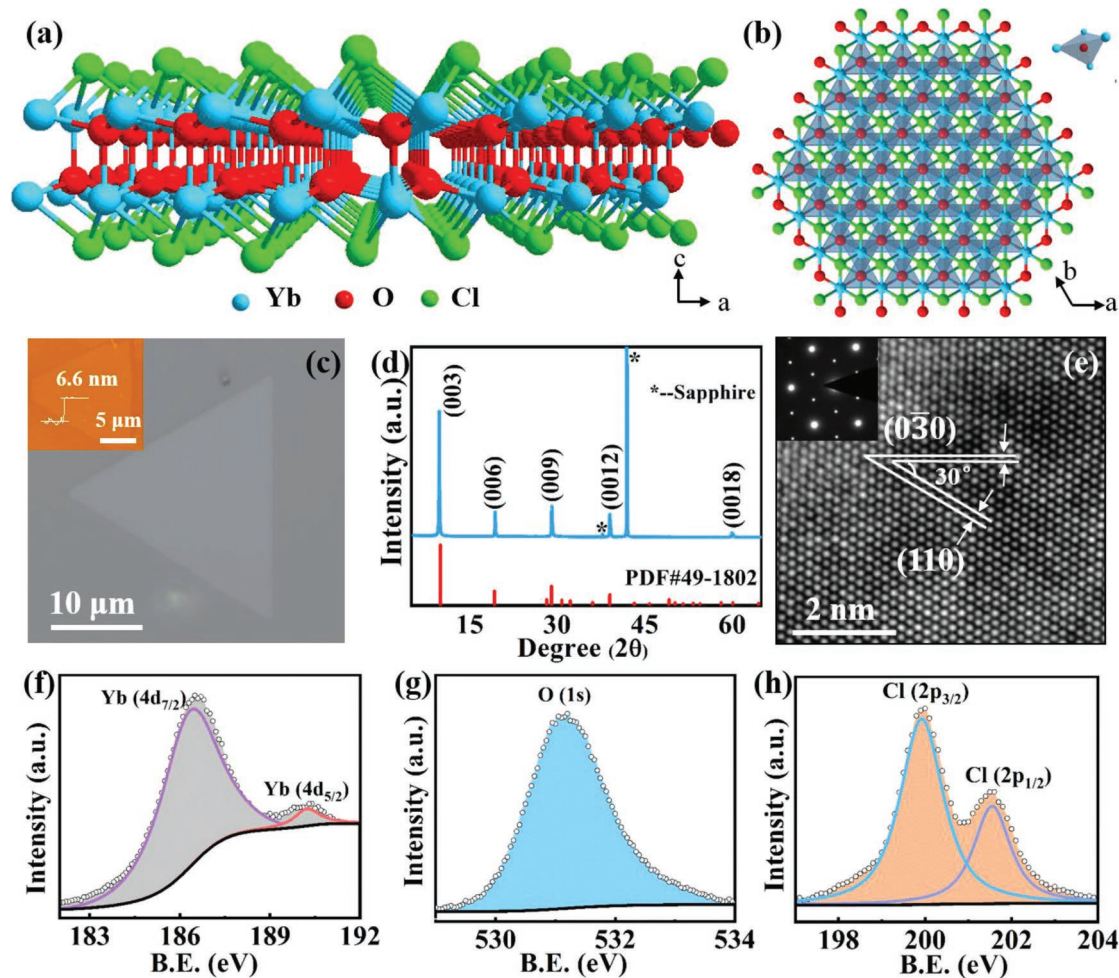


**Figure 1.** Structure, morphology and characterizations of 2D YbOCl nanosheets on sapphire substrates. a) Schematic of YbOCl crystal structure. b) Top-view of YbOCl crystal structure. Upper right corner of (b): Single  $[Yb_4O]$  tetrahedral unit. Blue ball: Yb; Red ball: O; Green ball: Cl. c) Typical OM image of as-grown YbOCl nanosheets on sapphire substrate, showing a regular triangle with the edge length of 23  $\mu\text{m}$ . Scale bar: 10  $\mu\text{m}$ . Inset: A representative AFM image of YbOCl nanosheets with thickness of 6.6 nm. Scale bar: 5  $\mu\text{m}$ . d) XRD profile for the YbOCl nanosheets on sapphire substrate. The asterisk represents the peaks of sapphire substrate. e) High-resolution TEM image of YbOCl nanosheets. Scale bar, 2 nm. Inset: Corresponding SAED pattern. f–h) XPS spectra of as-grown YbOCl nanosheets for Yb 4d, O 1s, and Cl 2p orbitals, respectively.

To investigate the effect of growth temperature on the growth behavior, we have further optimized the growth conditions. Keeping the other parameters (growth time, flow rate, etc.) constant, the YbOCl nanosheets were synthesized at different growth temperatures. Typical OM images of as-grown YbOCl nanosheets and their corresponding AFM images are presented in Figure S5 (Supporting Information), showing an obvious temperature dependence. The results reveal that higher temperature would provide a faster chemical reaction rate and more precursor supply to result in thicker nanosheets. And the size and thickness distribution histogram obtained at different temperature as shown in Figure S6 (Supporting Information). In this regard, an appropriate control of the growth parameters can efficiently modulate the growth results. Briefly, these results reveal that the ultrathin YbOCl nanosheets with high crystal quality were epitaxially grown on sapphire substrates through an APCVD method, which provide more opportunities for the next Raman study.

## 2.2. Theoretical Investigation of Raman Scattering of YbOCl

Notably, Raman scattering spectroscopy, an efficient and advanced technique, can characterize the mechanical, structural, and optical properties of 2D layered materials,<sup>[22,23]</sup> which has not been expanded to YbOCl single crystals in previous studies. First, we investigated the phonon dispersion of the bulk YbOCl using DFT calculations. The trigonal YbOCl single crystal belongs to the  $D_{3d}$  point group and  $R\bar{3}m$  space group. As shown in Figure 3a, bulk YbOCl has a total of 18 vibrational modes at the center of the Brillouin zone ( $\Gamma$  point). On the basis of the group theory, which are assigned as follows

$$\Gamma = 3A_{1g} + 3A_{2u} + 3E_u + 3E_g \quad (1)$$

$E_g$  and  $E_u$  are doubly degenerated phonon modes. Among those 18 vibrational modes, 9 of them are Raman active, which can be described as follows

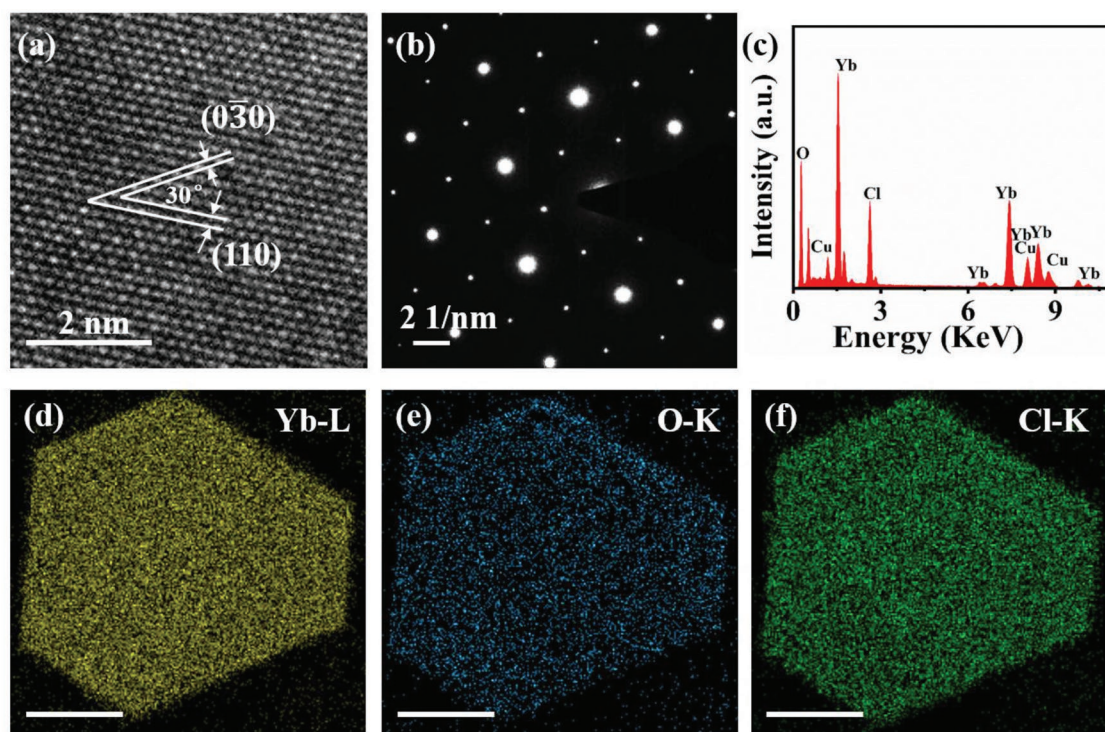


**Figure 2.** a) High-resolution TEM image of hexagonal YbOCl nanosheets. Scale bar, 2 nm. b) Corresponding SAED pattern of hexagonal YbOCl nanosheets. Scale bar, 2 1/nm c) Elemental analysis of hexagonal YbOCl nanosheets by EDS. d–f) Yb, O, and Cl elemental mappings, respectively, of the hexagonal YbOCl nanosheets. Scale bar, 5  $\mu\text{m}$ .

$$\Gamma = 3A_{1g} + 3E_g \quad (2)$$

The atomic displacement diagrams of these Raman active modes are presented in Figure 3b–g. The  $A_{1g}$  mode corresponds to the out-of-plane vibration while  $E_g$  mode denotes an in-plane atomic displacement. Furthermore, the  $E_g$  modes (84.6 and 168.5  $\text{cm}^{-1}$ ) and  $A_{1g}$  mode located at 139.6  $\text{cm}^{-1}$  attribute to the vibration of all atoms (Yb, O, and Cl) along in-plane and out-of-plane directions, respectively. The  $E_g$  mode at 419.8  $\text{cm}^{-1}$  emanates from the vibration of O and Cl atoms within in-plane direction, while the  $A_{1g}$  mode at 286.3  $\text{cm}^{-1}$  mainly originates from the vibration of Cl and Yb atoms along an out-of-plane direction. The  $A_{1g}$  mode located at 440.5  $\text{cm}^{-1}$  is related to the vibration of O atoms along c-axis. Overall, the theoretical calculations elaborate the Raman active modes of YbOCl crystals and their corresponding atomic displacement diagrams, which offer a fertile ground for further experimental investigation.

### 2.3. Experimental Investigation of Raman Scattering of YbOCl

Further, a series of Raman characterizations were performed on the as-grown YbOCl crystals to demonstrate the Raman characteristics through the experiment. All the Raman experiments were performed in a backscattering configuration. And the YbOCl samples were characterized by a micro-Raman spectrometer with a solid state green laser ( $\lambda = 532 \text{ nm}$ ) in the air. **Figure 4a** presents a typical Raman spectrum of the as-grown YbOCl nanosheets ranging from 50 to 200  $\text{cm}^{-1}$ .

Two prominent Raman modes are observed, located at 85.53 and 138.17  $\text{cm}^{-1}$ , respectively. The peak position can get from the peak fitting, which is shown in Figure S7 (Supporting Information). Evidently, the experimental Raman results well match to the  $E_g$  and  $A_{1g}$  modes obtained from the theoretical calculations. Additionally, the entire Raman spectra of YbOCl samples on the sapphire substrate and the  $\text{SiO}_2/\text{Si}$  substrate (Figure S8, Supporting Information) show that no extra  $E_g$  and  $A_{1g}$  modes are observed experimentally. Then we further did a series of experiments to confirm the number of Raman modes (Figures S9 and S10, Supporting Information), such as using thicker flake, using higher laser power, collecting the spectrum for longer acquisition times, increasing the accumulation time, and trying different excitation wavelengths. From these results, we can draw a conclusion that there are only two Raman modes can be detected for the YbOCl material. The probable reasons may come from selection rules for the scattering geometry<sup>[24]</sup> or the limited rejection of the Rayleigh scattered radiation.<sup>[25]</sup> Figure 4b,c exhibits the Raman mapping images constructed by integrating correlated Raman peak intensities ( $E_g$ : 85.53  $\text{cm}^{-1}$ ;  $A_{1g}$ : 138.17  $\text{cm}^{-1}$ ). The uniform contrasts indicate the uniform chemical distribution across the entire YbOCl nanosheet. Similarly, the Raman maps on hexagonal YbOCl nanosheets showing uniform intensities also confirm this result (Figure S11, Supporting Information). Temperature-dependent Raman scattering spectroscopy is an efficient characterization technique for studying the thermal conductivity and phonon behavior of 2D layered materials.<sup>[26,27]</sup> Figure 4d shows the Raman spectra for the triangular YbOCl crystals as a function of temperature from 77 to 270 K. As expected, the

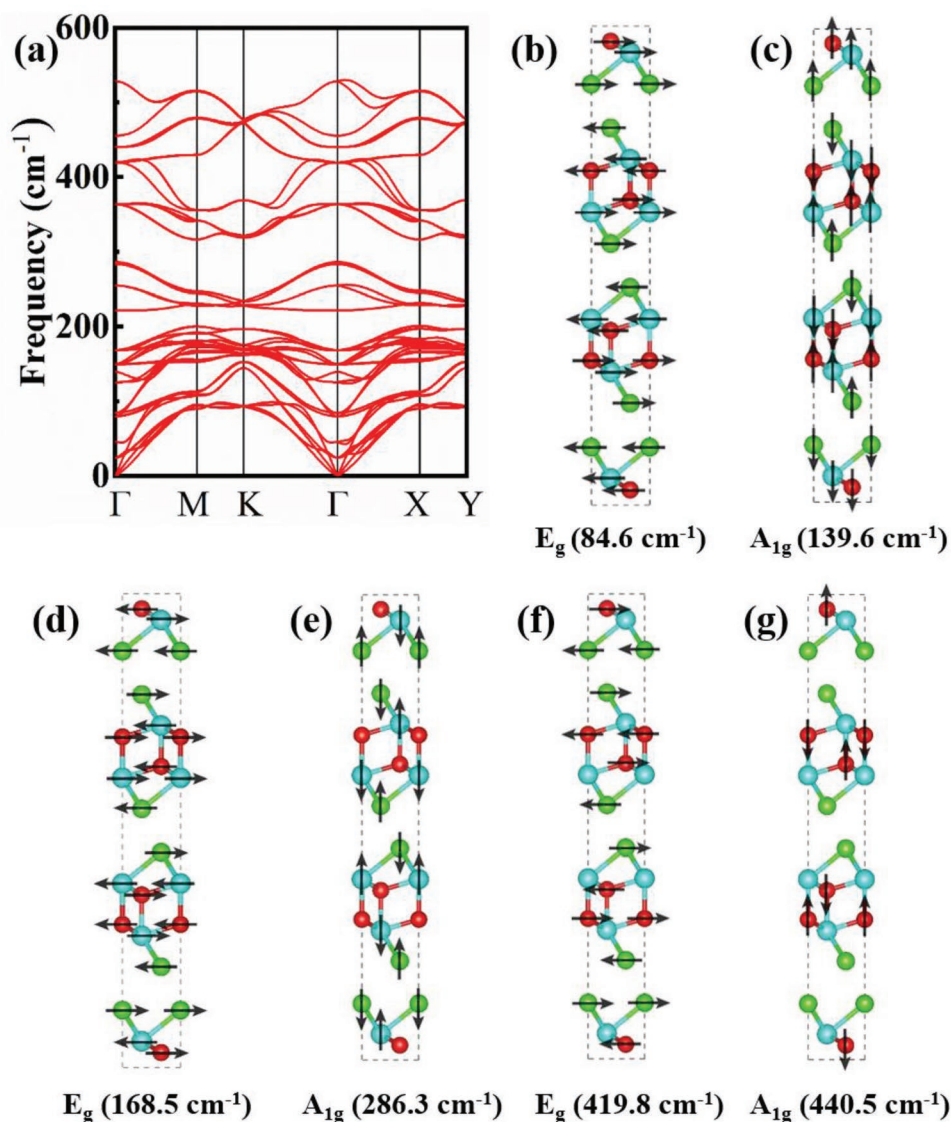


**Figure 3.** DFT calculation of phonon dispersion for bulk YbOCl single crystal. a) DFT-calculated phonon dispersion. b–g) Atomic displacement diagrams of all Raman active model. The dashed black lines outline the unit cells of the YbOCl single crystal. Blue ball: Yb; Red ball: O; Green ball: Cl.

typical Raman peaks exhibit a blueshift with decreasing the temperature. The dependence of these two Raman peak positions ( $E_g$  and  $A_{1g}$  modes) on the temperature is illustrated in Figure 4e, f. It can be seen that a linear dependence with the temperature range from 77 to 270 K is observed. Grüneisen model, commonly describing the temperature-dependence Raman shifts of various 2D materials,<sup>[28,29]</sup> can be used for the analysis

$$\omega(T) = \omega_0 + \chi T \quad (3)$$

where  $\omega_0$  is the phonon frequency at 0 K and  $\chi$  is the first order temperature coefficient of Raman modes. Thermal anharmonicity, consisting of thermal and volume contribution, is the main factor for the variation of the Raman modes.<sup>[30]</sup> And the thermal change of the crystal can induce an increase or decrease in the force constant, which eventually lead to a shift

in the peak positions of the Raman spectra. The change in Raman frequency can be given by<sup>[27,31]</sup>

$$\Delta\omega = (\chi_T + \chi_V)\Delta T = \left(\frac{d\omega}{dT}\right)_V \Delta T + \left(\frac{d\omega}{dV}\right)_T \Delta V \quad (4)$$

$$= \left(\frac{d\omega}{dT}\right)_V \Delta T + \left(\frac{d\omega}{dV}\right)_T \left(\frac{dV}{dT}\right)_P \Delta T \quad (5)$$

where  $\chi = \chi_T + \chi_V$ , and  $\chi_T$  is the self-energy shift caused by the interaction of phonon modes and  $\chi_V$  is the volume change caused by thermal expansion. Hence, according to this formula, the values of  $\chi$  for the YbOCl crystals, corresponding to the slope of the fitted line for  $E_g$  and  $A_{1g}$  modes (Figure 4e,f), are calculated as  $-(4.71 \pm 0.41) \times 10^{-3}$  and  $-(6.6 \pm 0.39) \times 10^{-3} \text{ cm}^{-1} \text{ K}^{-1}$ , respectively, which are a little smaller than other 2D layered materials. It has been reported

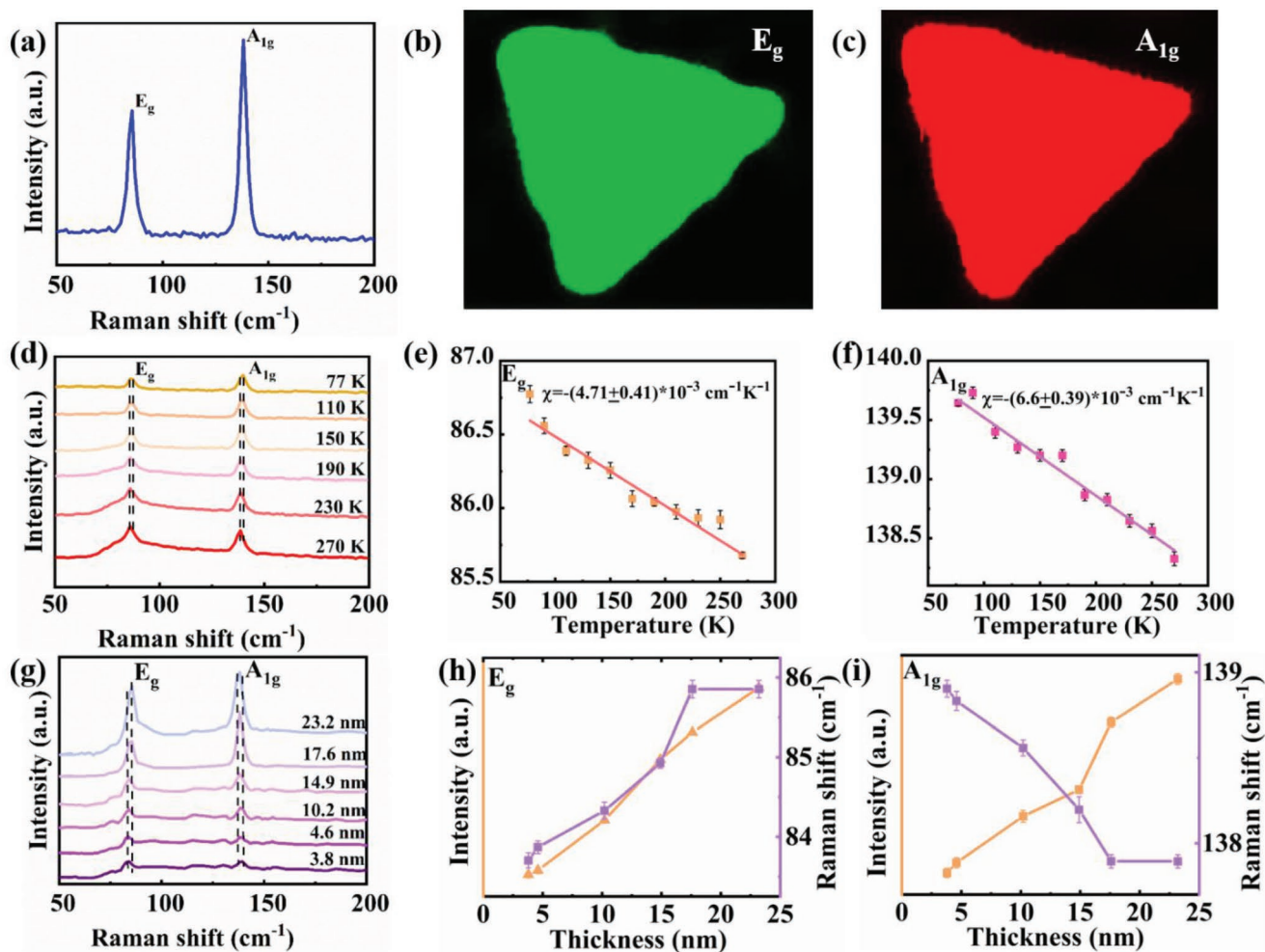


**Figure 4.** Temperature-dependent Raman spectra and thickness-dependent Raman spectra of triangular YbOCl nanosheets. a) Typical Raman spectra of triangular YbOCl nanosheets. b,c) 2D Raman mapping images based on the intensity of the  $E_g$  and  $A_{1g}$  modes. d) Temperature-dependent Raman spectra. e,f) Raman frequencies of  $E_g$  and  $A_{1g}$  modes as a function of temperature, respectively. The dots denote the experimental data, the linear lines corresponds to the fitting data. g) Thickness-dependent Raman spectra. h,i) The thickness dependence of Raman intensities (yellow curves) and Raman shifts (purple curves) of  $E_g$  and  $A_{1g}$  modes.

that the value of the  $\chi$  in the 2D layered material can reflect the magnitude of the vdWs interaction force between each layers.<sup>[32–34]</sup> Thus, the smaller  $\chi$  extracted from the Raman spectra reveals that YbOCl single crystal owns relatively weaker interlayer vdWs interactions than other 2D materials. And  $\chi$  value of other 2D materials is shown in Table S3 (Supporting Information). Besides, temperature-dependent Raman spectra of the hexagonal YbOCl nanosheets (Figure S12, Supporting Information) demonstrate the same tendency and similar  $\chi$  value for  $E_g$  and  $A_{1g}$  modes ( $-(4.21 \pm 0.41) \times 10^{-3} \text{ cm}^{-1} \text{ K}^{-1}$  and  $-(6.64 \pm 0.39) \times 10^{-3} \text{ cm}^{-1} \text{ K}^{-1}$ ).

Further the thickness-dependent Raman scattering analysis was also performed at room temperature. The Raman spectra in the range from 50 to 200  $\text{cm}^{-1}$  of YbOCl nanosheets are demonstrated in Figure 4g. It can be seen that two typical Raman modes ( $E_g$  and  $A_{1g}$  modes) constantly are observed with the thickness varying from 3.8 to 23.2 nm at room temperature, which exhibit visible shifts with increasing the thickness. The corresponding AFM images and height profiles

are shown in Figure S13 (Supporting Information). In detail, Figure 4h,i shows the vibration tendency of mode intensity and the Raman shift for  $E_g$  and  $A_{1g}$  modes as a function of thickness, respectively. Notably, the intensities of both peaks increase with increased thickness. Moreover, the Raman frequency of  $E_g$  mode also increases with increased thickness, whereas the Raman frequency of  $A_{1g}$  mode decreases. According to the classical model, the coupled harmonic oscillator's model, with increased thickness, the increased interlayer vdWs interaction of YbOCl single crystal would increase the effective forces acting on all atoms, which eventually suppress the vibration of atoms. Thus, the  $E_g$  and  $A_{1g}$  modes are in principle blueshifted. A blueshift of  $E_g$  mode for YbOCl single crystal with increased thickness is observed (Figure 4h), which is consistent with this prediction. In contrast, the  $A_{1g}$  mode shows a visible redshift (Figure 4i), which suggests that the interlayer vdWs interaction does not play a major role here. But the specific mechanism of this shift still needs a further intensive study.

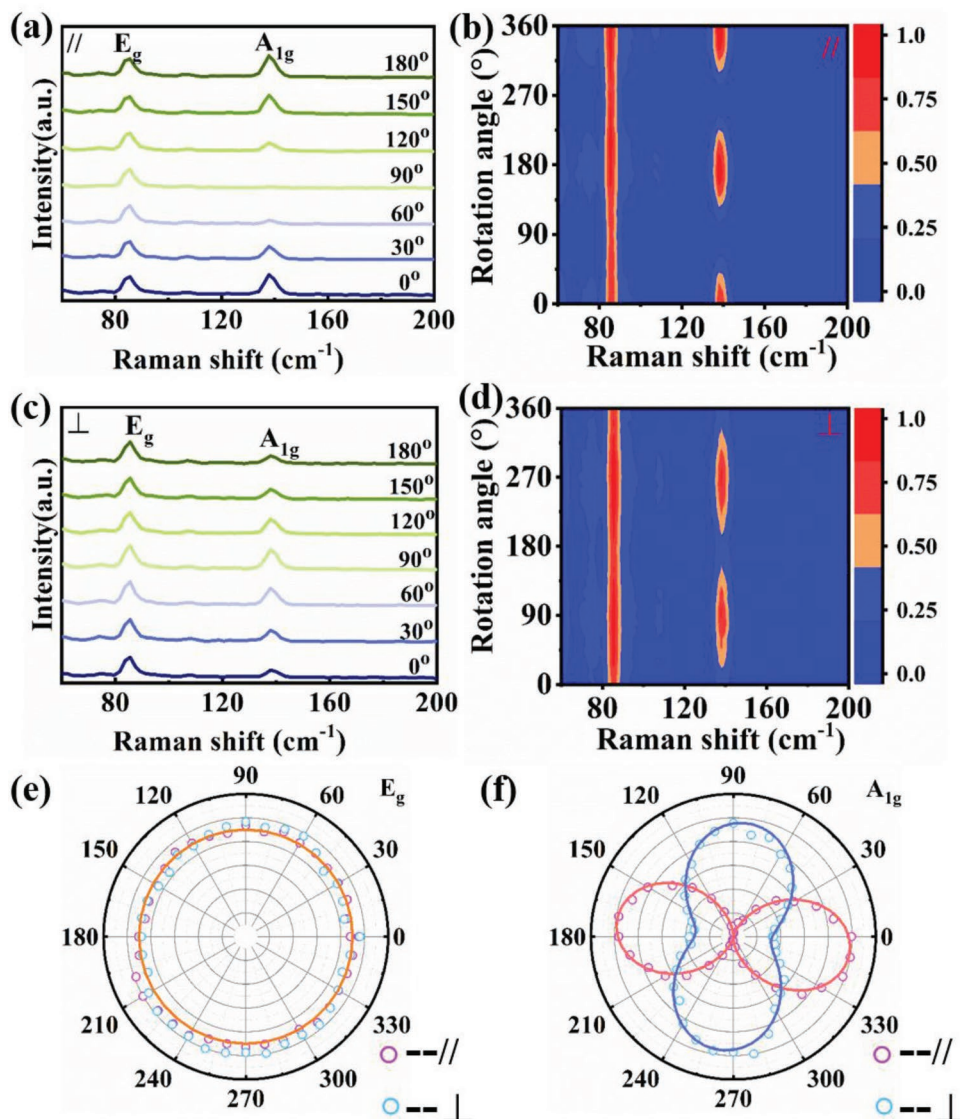


**Figure 5.** Angle-resolved polarized Raman scattering spectra of 2D triangular YbOCl nanosheets. a,c) Polarized Raman spectra of YbOCl triangular nanosheets under parallel configuration and cross-polarization configuration, respectively. b,d) False-color plot of the polarized Raman spectra of YbOCl triangular nanosheets under parallel configuration and cross-polarization configuration, respectively. The color scale indicates the intensity of the Raman vibration which has been normalized by maximum value. e,f) Polar plots of Raman frequencies of the  $E_g$  and  $A_{1g}$  modes as a function of rotation angle for incident light. The radial axis represents the peak intensity while the polar axis denotes the rotational angle of the polarization. Purple circles correspond to experimental data under the parallel configuration, blue circles represent experimental data under cross-polarization configuration. The colored solid lines refer to the fitting data.

Furthermore, angle-resolved polarized Raman scattering measurement was also performed on YbOCl crystals under parallel and cross-polarization configuration. Basically, it is considered as an effective method to characterize the symmetry of the crystal structure and the vibrational modes of 2D layered material.<sup>[35–37]</sup> During the angle-resolved polarized Raman characterization, the YbOCl sample kept stationary and the polarizer in front of the detector was set to selectively receive the scattering light. And then the angle-resolved polarized Raman spectra were obtained by controlling the half wave plate of the incident laser beam. **Figure 5a,c** depicts the polarized Raman spectra of an

as-grown 2D triangular YbOCl sample at different rotation angles under parallel and cross-polarization configuration, respectively. The intensities of  $A_{1g}$  mode in the spectra were found to periodically change with varying in the rotation angles in both configurations. In the contrary, the intensity of  $E_g$  mode shows no change with different rotation angles. And the corresponding maps of angle-dependent Raman scattering spectra (**Figure 5b,d**) clearly show the periodic change of the Raman intensity for each mode. These intensities are represented by the color scale shown on the right side of the figures, which have been normalized by maximum value. Further, the polar plots of the Raman intensity

as a function of the rotation angle for  $E_g$  and  $A_{1g}$  modes are shown in Figure 5e,f. It can be seen that the intensity of  $A_{1g}$  mode exhibits twofold patterns with the rotation angles, where the maximum intensities occur almost at  $\theta = 0^\circ$  and  $\theta = 90^\circ$  for parallel configuration and cross-polarization configuration, respectively. Differently, the Raman intensity of  $E_g$  mode does not show obvious change along with the rotation angles. According to the selection rules, the intensity ( $I_s$ ) of Raman-active modes depend on the Raman tensor  $\mathbf{R}$ , the polarization of the incident radiation and the scattered radiation, which can be written as

$$I_s \propto \sum_i |\bar{\mathbf{e}}_i \cdot \mathbf{R} \cdot \bar{\mathbf{e}}_s| \quad (6)$$

where,  $\bar{\mathbf{e}}_i$  and  $\bar{\mathbf{e}}_s$  are the polarization vectors for the incident and scattered photons, respectively. In the backscattering configuration, the initial  $\bar{\mathbf{e}}_i$  is set as (1 0 0). When polarization direction is rotated by  $\theta^\circ$ ,  $\bar{\mathbf{e}}_i$  can be written as ( $\sin\theta \cos\theta$  0), while  $\bar{\mathbf{e}}_s$  is fixed at (1 0 0) and (0 1 0) for the parallel and cross-polarization configurations, respectively. The form of  $\mathbf{R}$  is determined by the point group and the symmetry of structure according to the group theory. As mentioned above, the YbOCl single crystal behaves as a trigonal symmetry belonging to the point group  $D_{3d}$ . Hence, the Raman tensors can be denoted by a (3 × 3) matrix with nonzero elements  $a, b, c, d$

$$A_{1g}: \begin{pmatrix} a & 0 & 0 \\ 0 & a & 0 \\ 0 & 0 & b \end{pmatrix}$$

$$E_g: \begin{pmatrix} c & 0 & 0 \\ 0 & -c & d \\ 0 & d & 0 \end{pmatrix}, \begin{pmatrix} 0 & -c & -d \\ -c & 0 & 0 \\ -d & 0 & 0 \end{pmatrix}$$

Thus, the intensity of the  $A_{1g}$  and  $E_g$  Raman modes can be calculated as

$$I_{A_{1g}}^{\parallel} \propto a^2 \cos^2 \theta \quad (7)$$

$$I_{A_{1g}}^{\perp} \propto a^2 \sin^2 \theta \quad (8)$$

$$I_{E_g}^{\parallel} \propto c^2 \quad (9)$$

$$I_{E_g}^{\perp} \propto c^2 \quad (10)$$

For the  $E_g$  mode, whether in parallel configuration or cross-polarization configuration, its Raman intensity can be expressed as  $c^2$ , whereas the intensity of  $A_{1g}$  mode complies with Formulas (7) and (8), which is in accordance with the experimental result. In brief, these results clearly demonstrate the optical properties of as-synthesized YbOCl crystal. In addition, the angle-resolved polarized Raman scattering spectra of hexagonal YbOCl nanosheets were shown in Figure 6. From these results, we can see, the intensity of  $A_{1g}$  mode also exhibits twofold patterns with the rotation angles, but the intensity of  $E_g$  keeps constant, which show the similar results as the triangular ones.

### 3. Conclusion

In summary, we have successfully synthesized the high-quality, single-crystalline 2D layered YbOCl nanosheets with a thickness of sub-10 nm via a facile APCVD growth method. Both ultrathin hexagonal and triangular YbOCl nanosheets with identical crystal structures are obtained via an efficient control. The Raman properties of YbOCl as-grown nanosheets are systematically investigated by experimental measurements and theoretical calculations, for the first time. The experimental frequencies of  $E_g$  and  $A_{1g}$  modes were in accordance with calculated Raman results. The smaller first order temperature coefficient  $\chi$  of  $E_g$  and  $A_{1g}$  Raman modes reveals the YbOCl crystal possesses a relatively weaker interlayer interaction. Moreover, the angle-resolved polarized Raman measurement indicates the intensity of  $A_{1g}$  mode exhibits twofold patterns as the rotation angle changes, whereas the intensity of  $E_g$  mode keeps constant. We believe that this work paves the way for the controllable growth of new 2D materials.

### 4. Experimental Section

**Synthesis of 2D YbOCl Nanosheets:** High-quality 2D YbOCl nanosheets were obtained by chemical vapor transport method in a horizontal quartz tube furnace under atmospheric pressure. Ytterbium oxide ( $Yb_2O_3$ ) (0.5 g, Aladdin, purity 99.99%) powder and Ytterbium chloride hexahydrate ( $YbCl_3 \cdot 6H_2O$ ) powder (0.5 g, Energy Chemical, purity 99.99%) were used as precursors. These precursors were mixed evenly with a little amount of sodium chloride (NaCl) powder (0.05 g, Aladdin, purity 99.99%) in a quartz boat before loaded at the center of furnace. The sapphire ( $Al_2O_3$ ) substrates (Nanjing MKNANO Tech. Co., Ltd., www.mukenano.com) were faced downward on the mixed powder with the temperature of 730–800 °C. The furnace tube was then purged with 500 sccm Ar for 15 min before heating. After that, the flow rate was maintained at 120 sccm Ar which is a preferable growth atmosphere for the growth process. After 30 min of growth, the furnace was naturally cooled down to room temperature, and finally 2D YbOCl was obtained on sapphire substrates.

**Characterizations of As-Grown YbOCl Nanosheets:** The as-synthesized high-quality 2D YbOCl single crystal was characterized by OM (Olympus BX51M), AFM (Bruker dimension Icon), XPS (ESCALAB 250 Xi), XRD (Bruker, D8 Focus, Cu  $K\alpha$  line), HRTEM (Tecnai F20), SAED, and energy dispersive X-ray spectroscopy attached to the TEM, and Raman (Renishaw InVia, 532 nm excitation laser).

**Transfer of As-Grown YbOCl Nanosheets:** The as-grown YbOCl nanosheets on sapphire substrate were transferred onto carbon film-supported copper grid or  $SiO_2/Si$  substrate by PMMA (495 K, A4, Microchem Company)-assisted wet transfer process. Sapphire substrate with as-grown YbOCl nanosheets was spin-coated with PMMA solution at 2000  $r \min^{-1}$  for 45 s followed by drying on a heating plate at 120 °C for 10 min. Then the samples supported by PMMA film were peeled off by thin-tipped tweezer under the water, collected by a copper grid or  $SiO_2/Si$  substrate, and then heated at 100 °C until a good gluing between the film and the new substrate was obtained. Finally, the PMMA film was removed via dissolution with acetone for 30 min and dried by using  $N_2$  gas.

**Raman Spectroscopy Measurements:** All the Raman experiments were performed on a Renishaw InVia Raman microscope in a backscattering configuration. A solid state green laser ( $\lambda = 532$  nm) was used in air ambient environment. The laser, with 15 mW laser power, was focused on an  $\approx 1 \mu m^2$  area using a 100 × objective. The sample remained stationary and the polarizer in front of the detector was set to selectively receive the scattering light. For the parallel configuration, the polarization direction of the incident laser beam was parallel to the polarization direction of the scattered light. Similarly, for the cross-polarization configuration,

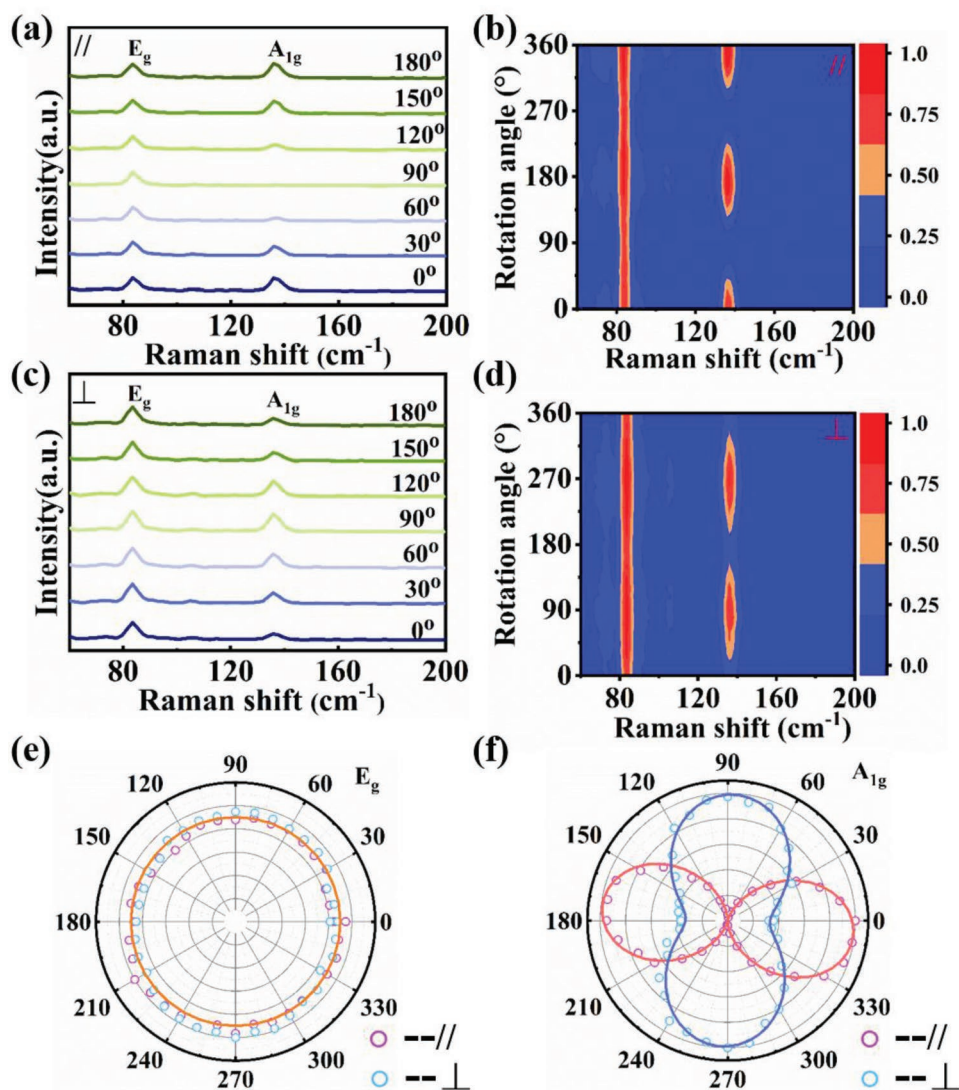


**Figure 6.** Angle-resolved polarized Raman scattering spectra of 2D hexagonal YbOCl nanosheets. a,c) Polarized Raman spectra of YbOCl hexagonal nanosheets under parallel configuration and cross-polarization configuration, respectively. b,d) False-color plot of the polarized Raman spectra of YbOCl hexagonal nanosheets under parallel configuration and cross-polarization configuration, respectively. The color scale indicates the intensity of the Raman vibration which has been normalized by maximum value. e,f) Polar plots of Raman frequencies of the  $E_g$  and  $A_{1g}$  modes as a function of rotation angle for incident light. The radial axis represents the peak intensity while the polar axis denotes the rotational angle of the polarization. Purple circles correspond to experimental data under the parallel configuration. The colored solid lines refer to the fitting data.

the polarization direction of the incident laser beam was vertical to the polarization direction of the scattered light. The angular-dependence Raman spectra response was obtained by controlling the half wave plate of the incident laser, which was used to change the polarization direction of the light.

**Theoretical Calculation:** DFT calculations were performed by using Vienna Ab Initio Simulation Package (VASP). The electron-ion potential and exchange-correlation functional were treated by projected augmented wave and generalized gradient approximation, respectively. For the electronic structures calculations, the kinetic energy cutoff was set to 500 eV. The  $k$ -point meshes of  $7 \times 7 \times 2$  and  $7 \times 7 \times 1$  were used to optimize the geometric structures of bulk and monolayer YbOCl crystals. The vacuum region of 20 Å was used to avoid the periodic interaction. The stress force and energy convergence criterions were chosen as 0.01 eV Å<sup>-1</sup> and 10<sup>-5</sup> eV, respectively. The vdWs force was treated by a semiempirical DFT-D3 method. Additionally, the PHONOPY code was

used to calculate the phonon spectrum and vibration modes of bulk YbOCl. Based on the density functional perturbation theory, the  $3 \times 3 \times 1$  supercell and adopt the  $5 \times 5 \times 1$   $k$ -point were used.

## Supporting Information

Supporting Information is available from the Wiley Online Library or from the author.

## Acknowledgements

Y.Y. and Y.Z. contributed equally to this work. This work was supported by Ministry of Science and Technology of China (No. 2016YFA0200700),

National Natural Science Foundation of China (Nos. 61625401, 21703047, 61574050, and 11674072), Strategic Priority Research Program of the Chinese Academy of Sciences (Grant No. XDA09040201), and CAS Key Laboratory of Nanosystem and Hierarchical Fabrication. The authors also gratefully acknowledge the support of Youth Innovation Promotion Association CAS.

## Conflict of Interest

The authors declare no conflict of interest.

## Keywords

2D layered material, chemical vapor deposition, density functional theory, Raman scattering, YbOCl

Received: April 15, 2019

Revised: July 21, 2019

Published online:

- [1] O. Lopez Sanchez, D. Lembke, M. Kayci, A. Radenovic, A. Kis, *Nat. Nanotechnol.* **8**, 497.
- [2] M. Massicotte, P. Schmidt, F. Violla, K. G. Schadler, A. Reserbat-Plantey, K. Watanabe, T. Taniguchi, K. J. Tielrooij, F. H. L. Koppens, *Nat. Nanotechnol.* **2016**, *11*, 42.
- [3] B. Radisavljevic, A. Radenovic, J. Brivio, V. Giacometti, A. Kis, *Nat. Nanotechnol.* **2011**, *6*, 147.
- [4] R. Cheng, F. Wang, L. Yin, K. Xu, T. A. Shifa, Y. Wen, X. Zhan, J. Li, C. Jiang, Z. Wang, *Appl. Phys. Lett.* **2017**, *110*, 173507.
- [5] N. Mounet, M. Gibertini, P. Schwaller, D. Campi, A. Merkys, A. Marrazzo, T. Sohier, I. E. Castelli, A. Cepellotti, G. Pizzi, *Nat. Nanotechnol.* **2018**, *13*, 246.
- [6] T. Low, P. Avouris, *ACS Nano* **2014**, *8*, 1086.
- [7] K. S. Novoselov, A. K. Geim, S. V. Morozov, D. Jiang, Y. Zhang, S. V. Dubonos, I. V. Grigorieva, A. A. Firsov, *Science* **2004**, *306*, 666.
- [8] T. Ohta, A. Bostwick, T. Seyller, K. Horn, E. Rotenberg, *Science* **2006**, *313*, 951.
- [9] M. Massicotte, P. Schmidt, F. Violla, K. Watanabe, T. Taniguchi, K. J. Tielrooij, F. H. L. Koppens, *Nat. Commun.* **2016**, *7*, 12174.
- [10] H. Huang, J. Wang, W. Hu, L. Liao, P. Wang, X. Wang, F. Gong, Y. Chen, G. Wu, W. Luo, *Nanotechnology* **2016**, *27*, 445201.
- [11] W. Wang, A. Klots, D. Prasai, Y. Yang, K. Bolotin, J. Valentine, *Nano Lett.* **2015**, *15*, 7440.
- [12] H. R. Gutierrez, N. Peralopez, A. L. Elias, A. Berkdemir, B. Wang, R. Lv, F. Lopezurias, V. H. Crespi, H. Terrones, M. Terrones, *Nano Lett.* **2013**, *13*, 3447.
- [13] Q. Guo, A. Pospischil, M. A. Bhuiyan, H. Jiang, H. Tian, D. B. Farmer, B. Deng, C. Li, S. Han, H. Wang, *Nano Lett.* **2016**, *16*, 4648.
- [14] J. Chu, F. Wang, L. Yin, L. Lei, C. Yan, F. Wang, Y. Wen, Z. Wang, C. Jiang, L. Feng, *Adv. Funct. Mater.* **2017**, *27*, 1701342.
- [15] J. Wu, H. Yuan, M. Meng, C. Chen, Y. Sun, Z. Chen, W. Dang, C. Tan, Y. Liu, J. Yin, *Nat. Nanotechnol.* **2017**, *12*, 530.
- [16] J. Li, Z. Wang, Y. Wen, J. Chu, L. Yin, R. Cheng, L. Lei, P. He, C. Jiang, L. Feng, *Adv. Funct. Mater.* **2018**, *28*, 1706437.
- [17] J. Wu, C. Tan, Z. Tan, Y. Liu, J. Yin, W. Dang, M. Wang, H. Peng, *Nano Lett.* **2017**, *17*, 3021.
- [18] N. Miao, B. Xu, L. Zhu, J. Zhou, Z. Sun, *J. Am. Chem. Soc.* **2018**, *140*, 2417.
- [19] W. Ouyang, F. Teng, X. Fang, *Adv. Funct. Mater.* **2018**, *28*, 1707178.
- [20] G. Brandt, R. Diehl, *Mater. Res. Bull.* **1974**, *9*, 411.
- [21] J. Zhou, J. Lin, X. Huang, Y. Zhou, Y. Chen, J. Xia, H. Wang, Y. Xie, H. Yu, J. Lei, *Nature* **2018**, *556*, 355.
- [22] X. Zhang, X. Qiao, W. Shi, J. Wu, D. Jiang, P. Tan, *Chem. Soc. Rev.* **2015**, *44*, 2757.
- [23] J. Wu, M. Lin, X. Cong, H. Liu, P. Tan, *Chem. Soc. Rev.* **2018**, *47*, 1822.
- [24] J. L. Verble, T. J. Wieting, *Phys. Rev. Lett.* **1970**, *25*, 362.
- [25] J. L. Verble, T. J. Wieting, P. R. Reed, *Solid State Commun.* **1972**, *11*, 941.
- [26] R. Yan, J. R. Simpson, S. Bertolazzi, J. Brivio, M. Watson, X. Wu, A. Kis, T. Luo, A. R. H. Walker, H. G. Xing, *ACS Nano* **2014**, *8*, 986.
- [27] I. Calizo, A. A. Balandin, W. Bao, F. Miao, C. N. Lau, *Nano Lett.* **2007**, *7*, 2645.
- [28] E. S. Zouboulis, M. Grimsditch, *Phys. Rev. B* **1991**, *43*, 12490.
- [29] M. Thripuranthaka, R. V. Kashid, C. S. Rout, D. J. Late, *Appl. Phys. Lett.* **2014**, *104*, 081911.
- [30] D. Yoon, Y. Son, H. Cheong, *Nano Lett.* **2011**, *11*, 3227.
- [31] A. Taube, A. Łapinska, J. Judek, M. Zdrojek, *Appl. Phys. Lett.* **2015**, *107*, 013105.
- [32] S. Luo, X. Qi, H. Yao, X. Ren, Q. Chen, J. Zhong, *J. Phys. Chem. C* **2017**, *121*, 4674.
- [33] A. Taube, A. Łapinska, J. Judek, M. Zdrojek, *Appl. Phys. Lett.* **2015**, *107*, 013105.
- [34] D. J. Late, S. N. Shirodkar, U. V. Waghmare, V. P. Dravid, C. N. R. Rao, *ChemPhysChem* **2014**, *15*, 1592.
- [35] H. B. Ribeiro, M. A. Pimenta, C. J. S. De Matos, R. L. Moreira, A. S. Rodin, J. D. Zapata, E. A. De Souza, A. H. C. Neto, *ACS Nano* **2015**, *9*, 4270.
- [36] S. Zhang, N. Mao, N. Zhang, J. Wu, L. Tong, J. Zhang, *ACS Nano* **2017**, *11*, 10366.
- [37] T. M. G. Mohiuddin, A. Lombardo, R. Nair, A. Bonetti, G. Savini, R. Jalil, N. Bonini, D. M. Basko, C. Galotit, N. Marzari, *Phys. Rev. B* **2009**, *79*, 205433.